

# Fully Printed Infrared Photodetectors from PbS Nanocrystals with Perovskite Ligands

AmirAbbas YousefiAmin,<sup>†</sup> Niall A. Killilea,<sup>†</sup> Mykhailo Sytnyk,<sup>†</sup> Philipp Maisch,<sup>‡</sup> Ka Cheong Tam,<sup>§</sup> Hans-Joachim Egelhaaf,<sup>§</sup> Stefan Langner,<sup>‡</sup> Tobias Stubhan,<sup>§</sup> Christoph J. Brabec,<sup>‡</sup> Tobias Rejek,<sup>||</sup> Marcus Halik,<sup>||</sup> Katharina Poulsen,<sup>⊥</sup> Jan Niehaus,<sup>⊥,∇</sup> Anton Köck,<sup>#</sup> and Wolfgang Heiss<sup>\*,†,ⓑ</sup>

<sup>†</sup>Institute - Materials for Electronics and Energy Technology, Department of Materials Science and Engineering, Friedrich-Alexander-Universität Erlangen-Nürnberg, Energy Campus Nürnberg, Fürtherstraße 250, D-90429 Nürnberg, Germany

<sup>‡</sup>Institute - Materials for Electronics and Energy Technology, Department of Materials Science and Engineering, Friedrich-Alexander-Universität Erlangen-Nürnberg, Martensstraße 7, D-91058 Erlangen, Germany

<sup>§</sup>Bavarian Center for Applied Energy Research (ZAE Bayern), Energy Campus Nürnberg, Fürther Straße 250, D-90429 Nürnberg, Erlangen Germany

<sup>||</sup>Institute of Polymer Materials, Department of Materials Science and Engineering, Friedrich-Alexander-University Erlangen-Nürnberg, Martensstrasse 7, D-91058 Erlangen, Germany

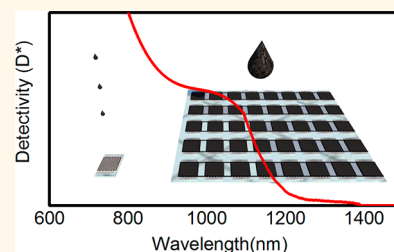
<sup>⊥</sup>Centrum für Angewandte Nanotechnologie (CAN) GmbH i. L., Grindelallee 117, D-20146 Hamburg, Germany

<sup>#</sup>Materials Center Leoben Forschung GmbH, Roseggerstraße 12, A-8700 Leoben, Austria

## Supporting Information

**ABSTRACT:** Colloidal nanocrystals from PbS are successfully applied in highly sensitive infrared photodetectors with various device architectures. Here, we demonstrate all-printed devices with high detectivity ( $\sim 10^{12}$  cm Hz<sup>1/2</sup>/W) and a cut-off frequency of >3 kHz. The low material consumption (<0.3 mg per detector) and short processing time (14 s per detector) enabled by the automated printing promises extremely low device costs. To enable all-printed devices, an ink formulation was developed based on nanocrystals stabilized by perovskite-like methylammonium iodobismuthate ligands, which are dispersed in a ternary solvent. Fully inkjet printed devices based on this solvent were achieved with printed silver electrodes and a ZnO interlayer. Considerable improvements were obtained by the addition of small amounts of the polymer poly(vinylpyrrolidone) to the ink. The polymer improved the colloidal stability of the ink and its film-formation properties and thus enabled the scalable printing of single detectors and detector arrays. While photoconductors were shown here, the developed ink will certainly find application in a series of further electronic devices based on nanocrystals from a broad range of materials.

**KEYWORDS:** colloidal nanocrystals, infrared detectors, inkjet printing, PbS, solution processing



The development of suitable functional electronic inks enabled the prospering of printed electronics, which is implemented in commercial products used by almost everyone: printed antennas<sup>1,2</sup> and sensors<sup>3,4</sup> are applied in the automotive industry in large quantities; in health care, printed electronics are used primarily in diagnostics<sup>5–7</sup> and in cell phones and television screens, printed organic light-emitting diodes<sup>8,9</sup> are implemented. While printed electronics was originally driven primarily by the application of organic semiconductors,<sup>10,11</sup> there is now also a vivid development of inorganic compounds for solution processed electronics.<sup>12</sup> Primarily, metallic nanocrystals were demonstrated for printed conducting strip lines.<sup>12–14</sup> The first all-inorganic electronic devices, namely field effect transistors fabricated by printing and made from CdSe colloidal nanocrystals, were introduced in 1999.<sup>15</sup> Nevertheless, there are still sparse examples of

printed devices based on semiconductor nanocrystals. Attempts have been made to provide Cu(In<sub>x</sub>Ga<sub>1-x</sub>)Se<sub>2</sub> inks for photovoltaic applications,<sup>16</sup> and by our group, inkjet-printed nanocrystal photodetectors have been demonstrated with a spectral range from the visible to wavelengths up to 3 μm.<sup>17</sup> While these devices showed rather limited performance with respect to specific detectivity, the newest developments of nanocrystal inks, based on PbS covered by metal halide perovskites,<sup>18</sup> pseudohalide, or halometallates,<sup>19</sup> are most promising, and they were shown to deliver outstanding results in solar cells<sup>20–22</sup> with the power conversion efficiency exceeding 10% and in field effect transistors, in which the

**Received:** December 5, 2018

**Accepted:** January 24, 2019

**Published:** February 1, 2019

nanocrystal layer is deposited in a single-step process.<sup>23</sup> Following the strategy of making use of metal halide perovskites to stabilize nanocrystals in polar solvents, here we introduce a nanocrystal ink of PbS nanocrystals stabilized by methylammonium iodobismuthate ligands<sup>24</sup> for the demonstration of an all-printed device in the form of a highly sensitive infrared photodetector. In particular, a combination of inkjet printing, 3D printing, and droplet dispensing is used to obtain detector arrays in a production time of a few minutes and with minimal waste of material. In particular, the photosensitive layer is prepared from a single droplet by making use of an optimized ink. The resulting detectors, which are fully prepared in ambient condition, exhibit a specific detectivity of up to  $2 \times 10^{12}$  cmHz<sup>1/2</sup>/W at room temperature, which is on par with the best state of the art infrared photodetectors operating within this wavelength region.<sup>25</sup>

## RESULTS AND DISCUSSION

The fabrication of fully printed devices requires a set of inks that allows a sequence of depositions on top of each other without damaging the layers beneath. The chosen printing processes should not only be simple and stable but also should allow the positioning of the functional materials on the substrate with sufficient resolution. The printing should be materially economical to reduce waste production and device costs as much as possible. Thus, we have chosen the following deposition sequence for the demonstration of photoconducting detectors (Figure 1a): Ag electrodes with several

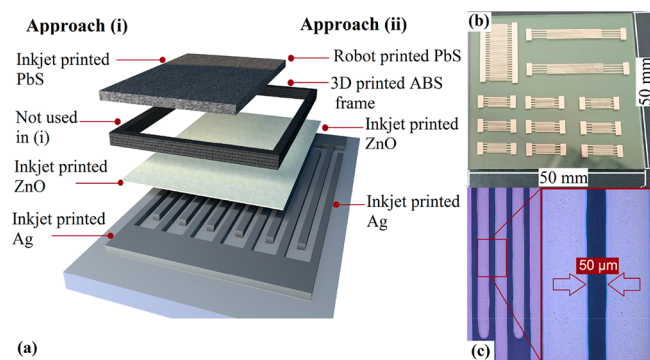


**Figure 1.** Fully printed nanocrystal photoconductors. (a) Sketch of the photoconducting devices prepared by two alternative all-printing approaches. (b) Interdigitate silver electrodes printed from a molecular precursor ink. (c) Electrode fingers with a distance of 50  $\mu\text{m}$  (the right image shows a zoom of the area surrounded by the red rectangular in the left image).

interdigitated fingers are inkjet-printed on glass substrates, enabling the application of an electrical bias in the lateral direction. On top of the finger electrodes and the gap space, a ZnO nanoparticle interlayer is inkjet-printed to prevent the microstructured silver electrodes from corrosion by the ink forming the photoconductive layer. The photosensitive nanocrystal layer is then deposited in two alternative ways. The first way that deposition makes use of inkjet printing of a multilayer of PbS nanocrystals with an appropriate surface functionalization (approach i in Figure 1a). Alternatively, a 3D printer equipped with a heated print head for thermoplastic materials is used to print a polymer frame. PbS nanocrystal ink is subsequently deposited inside the frame using a robot-controlled droplet dispenser, providing the desired ink volume

in a single shot (approach ii in Figure 1a). In the following, we describe in detail the printing of the metallic electrodes with a protective ZnO nanocrystal interlayer and an formulation of the PbS nanocrystal ink, which is sufficient to obtain single fully inkjet printed devices. After demonstrating the photoconductive properties of such a single device, we will introduce a route toward the scaling up of the printing. A modification of the ink will be described to obtain smooth and highly photosensitive films from single droplet depositions. This improved ink allows the application of an automated droplet dispenser for nanocrystal deposition on detector arrays. The optoelectronic properties of the detectors are reported in the last paragraph before the results will be summarized.

**Inkjet-Printed Electrode Structures.** For the printing of electrodes several metal inks are commercially available, but predominantly silver inks are in use. In this work, a conducting ink based on single-crystal silver nanoparticles in diethylene glycol monomethyl ether was used (Sicrys I40DM-106) and is sintered into a highly conducting film after deposition.<sup>26</sup> The whole electrode was printed in a single step, fast enough that the final pattern was present after the printing as a wet, liquid film. In the liquid phase, the surface tension results in a homogenization and smoothing of the film surface. After the printing was completely finished, the electrodes were solidified by drying at 150  $^{\circ}\text{C}$  for 10 min. Electrodes with several geometries were deposited in a single run and on a single glass substrate from a “Spectra S-Class” print-head with 128 nozzles (PiXDRO LP50). To avoid inhomogeneities of the electric field caused by varying distances between the electrodes, a single nozzle was used to print electrode structures with uniform gaps down to 50  $\mu\text{m}$  (Figure 1c). This distance is larger than what is obtained by optical lithography, usually used for electrode preparation. Nevertheless, as shown below, detectors with relatively high detectivity are obtained with these electrodes. The provided electrodes had a somewhat inhomogeneous thickness. At the border, they showed a 200 nm thick rim due to a coffee stain boarder line, while in between the rims, the silver film was about 140 nm in thickness (Figure S1). Printing the PbS nanocrystal ink described below in detail on top of the electrodes resulted in a catastrophic destruction of the silver electrodes (Figure S2). Thus, a protective layer of ZnO nanoparticles (N10-Nanograde)<sup>27</sup> was printed on top of the electrode structure, including the silver fingers and the gap regions in between the fingers. As a side effect, the ZnO layer resulted in a reduced dark current due to its hole-blocking nature.<sup>28,29</sup> However, the  $\sim 20$  nm thick nanoparticle film did not decrease the current measured under white-light illumination, as was proven on lithographically prepared gold electrodes (Figure S3).

**PbS Nanocrystal ink.** The crucial step to obtain fully printed nanocrystal photodetector devices is the preparation of the ink, which will provide the photosensitive layer. It should not only absorb in the infrared spectral region but also provide sufficiently high electron mobility to allow efficient charge separation by the applied electric field. Thus, the oleic-acid capped as synthesized PbS nanocrystals are not suitable for device fabrication. It is required to replace the almost insulating alkyl chains of the oleate ligands by much shorter species, which allow sufficient charge transport. Indeed, the list of tested ligands, which can be used to replace the oleic acid ligands after deposition of the nanocrystals to electronically couple them among each other, is rather extensive.<sup>30–34</sup>

However, there are much fewer species that can be used for replacements in solution, delivering both colloidal stability and high conductivity after film preparation. With respect to solar cells, very impressive power conversion efficiencies were obtained by making use of  $\text{CH}_3\text{NH}_3\text{PbI}_3$  perovskite type of ligands.<sup>22</sup> Similar to these ligands, our group recently suggested making use of  $\text{BiI}_6^{3-}$  clusters with methylammonium counterions for the ligand exchange procedure.<sup>24</sup> With these ligands, an epitaxial relation between the ligand shell and the PbS core material could be evidenced, and with the iodo-bismuthate-based ligands attached to the PbS nanocrystals, their luminescence became completely quenched. This quenching we attributed to a type II staggered band alignment between the PbS core and the quasi-epitaxial ligand shell, which is beneficial to obtain a fast charge separation after the photoexcitation of the nanocrystal solid and resulted in attractive photoconducting properties. An advantage of the chosen iodo-bismuthate-based ligands in comparison to other previously tested metal-halide perovskite ligands is that they provide the smallest lattice mismatch ( $-1\%$ ) in respect to the PbS core,<sup>24</sup> which results in negligible strain. The applied ligand exchange procedure from oleic acid to  $\text{BiI}_6^{3-}$  was obtained by a rapid phase-transfer process from toluene to DMF, and it was found to be easily scalable. Thus, here we applied it to PbS nanocrystals, which were synthesized by a scalable continuous and microfluidic synthesis method, allowing us to also obtain large quantities of nanocrystals without any performance loss in comparison to samples obtained in small batches. While in our previous work, photoconducting devices were prepared from DMF solution by a multiple drop and dry process, here, we employed either inkjet printing or a single-step deposition to form the photoconducting films, requiring in both cases improvements in the ink formulation.

**Fully Inkjet Printed Nanocrystal Photodetectors.** Our first attempts to achieve fully printed photoconducting nanocrystal devices operating in the infrared were based on inkjet printing to obtain the photosensitive layers. For inkjet printing, we used a piezoelectric printing head (MJ-ATP-01-80-8MX from MicroFab) consisting of a glass capillary and an orifice of  $80\ \mu\text{m}$ , applicable for the printing of fluids with a viscosity less than  $20\ \text{cP}$ . DMF has a low viscosity of  $0.79\ \text{cP}$  (at  $25\ ^\circ\text{C}$ ),<sup>35</sup> which is below the range of a highly printable solution. Thus, we added DMSO (viscosity  $1.99\ \text{cP}$ )<sup>36</sup> to the DMF solution containing the PbS nanocrystals to increase viscosity. Furthermore, within a highly diluted regime of colloidal solutions the Einstein relation proposes an increase of viscosity with increasing nanocrystal volume fraction.<sup>37</sup> By increasing the PbS concentration to  $40\ \text{mg/mL}$ , the a viscosity of  $8\ \text{cP}$  was achieved. Dispersions with higher nanocrystal concentrations showed immediate formation of aggregates, causing rapid clogging of the print-head nozzles. Thus, in all of our experiments, the nanocrystal concentration was limited to  $40\ \text{mg/mL}$ . A more-advanced criterion with which to decide if the colloidal nanocrystal solutions are printable, the Ohnesorge number is often quoted, and it relates the liquid's viscosity to the square root of the liquid's density, the surface tension, and the drop diameter. Good values for printing are found in the range between  $0.1$  and  $1$ .<sup>38</sup> With our colloidal solutions, the surface energy was determined from contact-angle measurements (Figure S4), providing Ohnesorge numbers in the desired range for drop diameters up to  $93\ \mu\text{m}$ . Indeed, single-droplet ejection was achieved when the piezoelectric dispenser

was driven with  $20\ \mu\text{s}$  long pulses with an amplitude of  $75\ \text{V}$  (Figure 2a). The droplet deposition was optimized by variation

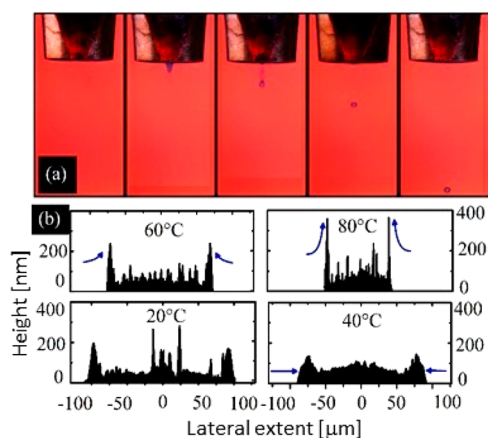


**Figure 2.** Printing of PbS nanocrystal ink. (a) Single-droplet ejection from a piezo-electrically driven nozzle with an orifice of  $80\ \mu\text{m}$ . (b) AFM cross-sections of printed droplets for different substrate temperatures.

of substrate temperature by evaluation of the deposited droplet homogeneity. A compromise with respect to the coffee-stain ring<sup>39</sup> formed at the perimeter of the droplet, and thickness fluctuations at regions within the droplet perimeter due to Marangoni flows and probably also hydrothermal waves occurring during solvent evaporation<sup>40</sup> were found for a substrate temperature of  $40\ ^\circ\text{C}$ . For this substrate temperature, the height of the coffee-stain ring is about  $170\ \text{nm}$ , the pronounced thickness maxima in the center of the disc almost vanished, and the averaged film thickness within the coffee stain ring increased to  $75\ \text{nm}$  (Figure 2b). By increasing the ejection rate and keeping the stage speed constant instead of using individual droplets, continuous lines were printed (Figure S5), and again, an optimized topography was found for a substrate temperature of  $40\ ^\circ\text{C}$  that was thus used throughout all following experiments.

Continuous nanocrystal films with appropriate thicknesses were then obtained by stacking several layers on top of each other. The printing was sufficiently stable to typically print 20 layers with a size of  $3\ \text{mm} \times 1\ \text{mm}$  on top of each other within a single printing run, providing a photoconducting nanocrystal film for one fully inkjet printed photodetector. After film formation and drying, another important reason for using a mixed solvent for dispersing the nanocrystals instead of a single one became apparent. If DMF is used as solvent only, then after the drying of the film, numerous cracks are observed within the nanocrystal layer and formed during solvent evaporation (Figure S6a). These cracks disable lateral charge transport and thus have to be avoided. When a binary solvent mixture DMF/DMSO (3:1) was used, no such cracks were observed, and surface roughness was substantially better (Figure S6b). Even-smoother layers were obtained by making use of a ternary solvent mixture (DMF/NMF/DMSO) with a composition of 2:1:1 (Figure S6c), which was then used for the printing of the PbS nanocrystals covered by iodobismuthate ligands. With the ternary ink, the fully inkjet printed photodetectors were functional. They exhibited a similar ratio of light off to light on to that of the reference sample printed on lithographically patterned finger structures (Figure S3). The responsivity spectrum of the fully printed device, shown in

Figure 3a, was measured with PbS nanocrystals with a size of 2–3 nm, exhibiting before the ligand exchange an excitonic

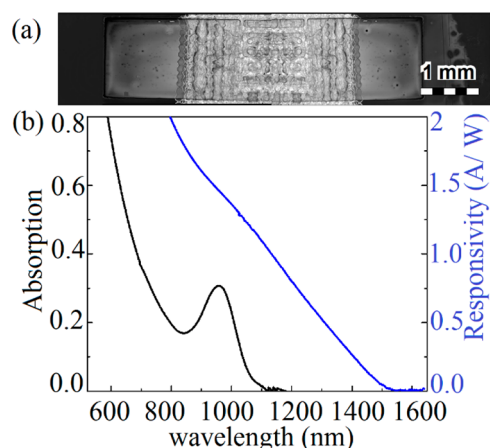


**Figure 3.** All-inkjet-printed photoconducting device. (a) Microscopic image of a fully printed photoconductor with 20 printed layers of PbS with Bil6-based ligands. (b) Absorption spectrum of the used nanocrystals with oleic acid ligands measured in tetrachloroethylene and the photoresponsivity spectrum of the device shown in panel a measured with a bias of 1.2 V/cm.

peak at 950 nm. From this excitonic absorption after ligand exchange and device printing, a small cusp remains; see Figure 3b. At this wavelength, the photoresponsivity spectrum exhibits a responsivity value of 1.5 A/W, which can be converted with the measured noise current of 20 pA and active detector area of 1 mm<sup>2</sup> to a specific detectivity of  $2 \times 10^{10}$  cm Hz<sup>1/2</sup>/W, measured at a repetition rate of 10 Hz. This value is within the range of detectivities found by other deposition techniques, thus showing the feasibility of inkjet printing for nanocrystal device preparation. However, the detectivity is smaller than what was obtained previously from drop-cast PbS nanocrystal photo-detectors by making use of the same methylammonium iodobismuthate ligand shell.<sup>24</sup> The inferior performance could be attributed to the larger electrode spacing (80 μm instead of 20 μm in ref 24 for lithographically prepared electrodes) and the larger film roughness of the inkjet printed film (rms = 64 nm; see Figure S7). However, there are additional characteristic to be considered that point to fundamental problems of the fully inkjet printed photodetector. (i) There is a considerable spectral shift between the cut-off wavelength measured in absorption and in the photoresponsivity spectrum, exhibiting signals up to 1500 nm (Figure 3b). This shift of 400 nm is twice as large as that observed in drop-cast nanocrystal detectors from the same material.<sup>24</sup> (ii) A photoresponsivity of 1.5 A/W can be achieved only with the presence of photoconductive gain. (iii) The fully inkjet printed detectors are very slow and exhibit a cutoff frequency of 1 Hz. These points indicate the presence of trap states, which could be formed because the devices are fabricated in air and exposed to elevated temperature for several minutes during the printing process. As discussed already in ref 41, the PbS nanocrystals are prone to be oxidized to PbSO<sub>4</sub> acting as traps in the nanocrystal devices. Thus, even though the full inkjet printing of nanocrystal-based photoconductors based on the used ternary solvent ink provides single devices, at the end, a better performance should be obtained. An additional complication with the inkjet printing is that the nanocrystal ink used here

shows a considerable shear force thickening (Figure S8), which causes frequent clogging of the inkjet nozzles, making the scaling up of the detector fabrication to large-area devices or detector arrays rather difficult. Thus, in the following, we present an alternative and strongly improved route toward all-printed nanocrystal photoconductors, providing better photoconducting properties as well as a facile scalability of the process.

**Improving Nanocrystal Ink with a Polymer.** While in the inkjet-printing approach described above, PbS nanocrystal films were obtained by the continuous addition of small liquid droplets to an already-dried pattern of previously deposited droplets, in the following, we attempt to provide a continuous nanocrystal film from a single, much-larger drop from a dispensing device. Deposition of a big drop of a nanocrystal solution based on DMF/NMF/DMSO deposited on glass resulted in a disc with a diameter of several millimeters. After drying at 40 °C, not only was a clear coffee-stain ring formed, but also, in the interior of the covered region, fragmented areas covered by layers of nanocrystals were separated by a fractal like pattern of cracks, with a wide range of dimensions (Figure 4a). Clearly, such a multiply cracked “film” is not appropriate

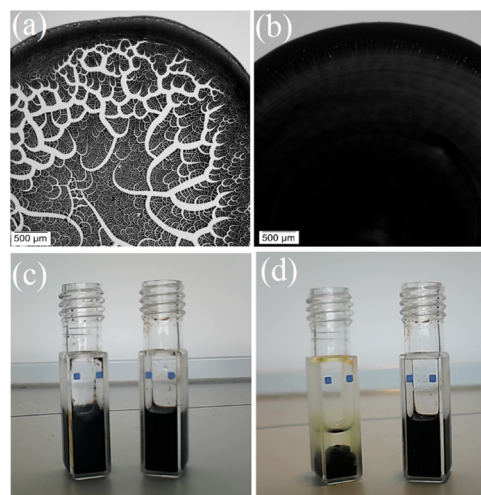


**Figure 4.** Nanocrystal ink modification. (a) Droplet of a 40 mg/mL PbS/BiI core/ligand shell nanocrystal ink dried on glass substrate from a DMF:NMF:DMSO mixture, exhibiting a fractal pattern of cracks. (b) Addition of PVP avoids any crack formation upon drying. (c) Improvement of colloidal stability. Cuvette on the left and right side is without and with, respectively, added PVP. (d) Results after 100 h.

for device fabrication because no current transport would be possible in lateral direction. Thus, an improvement of this property is required. In perovskite-based solar cells, a modification of the composition with polymers offering coordinating groups has been introduced recently, to significantly enhance the power conversion efficiency of semitransparent solar cells.<sup>42</sup> This approach was not restricted to the typical MAPbI<sub>3</sub> perovskites but was proven also to further perovskites, *e.g.*, the all-inorganic CsPbI<sub>3</sub>.<sup>43</sup> Because the nanocrystals used here exhibit a iodobismuthate-based perovskite ligand shell after ligand exchange, we attempted here to improve the properties of the nanocrystal ink by addition of the same polymer as was successfully applied in perovskite solar cells. Indeed, the addition of poly(4-vinylpyridine) (PVP) to the ternary ink formulation showed striking effects and

considerable improvements. First, the film formation upon droplet deposition on a glass slide was drastically changed. After the addition of PVP, a single drop deposition resulted in a uniformly dark coverage of the glass substrate without a single crack in the interior of the deposited area (Figure 4b). This single-step-deposited PVP-modified ink thus provides a film that is equivalent to those obtained by inkjet printing of multiple layers or by the frequently used layer-by-layer spin-casting approach combined with a solid-state ligand exchange procedure.<sup>44–46</sup> The second effect that the PVP addition provides is an increase of colloidal stability. After ligand exchange and solution in the ternary solvent, the nanocrystals with sizes of 2–3 nm are colloidally stable for less than 20 h, and a complete precipitation of the nanocrystals is observed after 100 h (Figure 4c,d). The PVP addition improves the colloidal stability markedly. After 100 h of storage in air, the colloidal solution did not show any signature of instability, and after 6 months, it is still stable. This improved stability is a result of the increased zeta potential, which we measured in the ternary solvent to be  $-20.5$  mV, whereas it is  $-53$  mV after the addition of PVP, suggesting that in this case, the stronger Coulomb repulsion is preventing aggregation of the nanocrystals. One problematic property of the nanocrystal solution in the ternary solvent remains also after the addition of the PVP, which is the shear force thickening, causing the clogging in the inkjet nozzle. The PVP addition resulted in a slight increase of viscosity, but a similar dependence on the shear rate was observed as without the PVP (Figure S8). After PVP addition, fully inkjet printed devices were fabricated and tested and indeed showed an improved characteristics compared to those without PVP in several respects: Single droplets and droplet lines and arrays could be deposited with improved topography (Figure S9). The responsivity spectrum of the devices showed a much more pronounced cusp close to the excitonic absorption peak, as measured in solution (Figure S10). The photoconductivity spectrum had a steeper drop at the long-wavelength side and ended at a wavelength closer to the excitonic absorption peak. The responsivity was lower than without PVP (Figure 3b) and was found in a range that can be obtained without contributions from photoconducting gain. Most importantly, the specific detectivity was higher,  $D^* = 6 \times 10^{11}$  cm<sup>1/2</sup>/W, for a device with the same dimensions of the silver electrodes as were used before with the nanocrystal ink without PVP. All of these properties point to a better nanocrystal film quality than without PVP with substantially fewer trap states affecting the photoconducting properties.

**Infrared Detectors from Scalable Printing.** Having established the superiority of the nanocrystal ink modified by polymer offering coordinating groups (PVP), the modified ink was applied to a technology enabling also the scalable printing of devices. For rapid printing, the photosensitive nanocrystal films were deposited in a single shot per device. In this case, the device pattern formation required an additional step to achieve the desired positioning of the deposited material, e.g., on top of the electrode structures. Thus, we have implemented printing a frame from a thermoplastic polymer by making use of a 3D printer. Important is in this respect that the used thermoplastic material cannot be dissolved in the solvent mixture used for nanocrystal deposition. We used an acrylonitrile butadiene styrene (ABS pro filament) for printing a 400  $\mu$ m high frame, which predefined the areas to be covered by the nanocrystals. For the deposition of the nanocrystal ink, we made use of a computer controlled robotic arm operating a

micropipette. On an  $8 \times 4$  array of interdigitate electrodes, the robot deposited the desired amount of 8  $\mu$ L of PbS nanocrystal ink for each device with a concentration of 40 mg/mL within 14 s per device (the device is shown in Figure 5a, and the

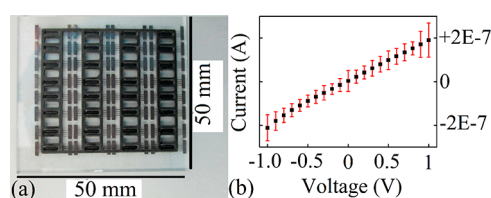


**Figure 5.** Fully printed photoconducting devices. The  $8 \times 4$  photoconducting devices in panel a provide under white-light illumination reproducible photocurrents, as shown by the error bars in panel b.

printing process is shown in Video S1). In comparison to that, the fully inkjet printing approach was more than 10 times slower (3 min per detector for this size). Furthermore, scaling to larger device numbers by inkjet printing was rather impossible due to frequent clogging of the printing nozzle. The automatized deposition by drop dispensing resulted in smooth film surfaces (rms = 21 nm; Figure S11a) and a high reproducibility, as was evidenced by the measured device current obtained under white light illumination. The error bars in Figure 5b indicate the variance of the results for 32 devices, which were printed on a single substrate. It should be noted that this printing technique is not restricted to such small detectors as shown here, but size scaling is straightforward (a 25 cm<sup>2</sup> single detector is shown, e.g., in Figure S11b).

To test the quality of the all printed photodetectors, we measured the spectral responsivity, which expands here to approximately 1200 nm, showing a shoulder at 1050 nm (Figure 6). This shoulder we attribute again to the exciton

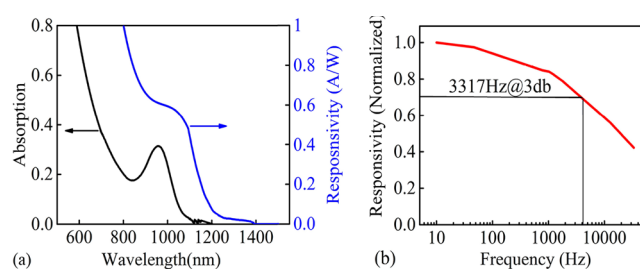


**Figure 6.** (a) Responsivity of the fully printed photoconductors compared to the absorbance measured in solution when capped with oleic acid ligands. The scale on the right side provides the detectivity, measured with a frequency of 1400 nm. (b) Frequency dependence of the responsivity showing a cutoff frequency of 3317 Hz.

ground-state transition, which is very pronounced in absorption measurements in solution performed prior to the ligand exchange procedure. The shoulder in the photoconductivity is still slightly red-shifted with respect to the absorption in solution, which indicates an electronic coupling of the nanocrystals in the film, probably related also with the type II band alignment between the PbS nanocrystal core and the BiI-based perovskite ligand shells.<sup>24</sup> The PVP addition to the ternary solvent resulted in the device in a reduced dark current (Figure S12) and, thus, noise. With the measured noise spectral density of 0.52 pAHz<sup>-1/2</sup> for a device area of  $\sim 0.8$

mm<sup>2</sup>, the specific detectivity obtained here is in excess of  $2 \times 10^{12}$  cmHz<sup>1/2</sup>/W at the wavelength of the excitonic shoulder and a frequency of 10 Hz, and it is substantially higher at shorter wavelengths. The photocurrent exhibits also a linear behavior as a function of light intensity (Figure S13) and a cut-off frequency of 3317 Hz (Figure 6b), which is considerably high for a photoconductor with lateral contacts and an active device widths of 80 μm. These values are excellent compared with devices prepared by other techniques.<sup>47–50</sup> Also, the stability of the printed photoconductors is comparably good in comparison with other PbS nanocrystal devices. In particular, we observe after 3 month storage in air a decrease of the photocurrent by approximately 50% (Figure S14), which is acceptable, considering that even commercial single crystal detectors are encapsulated in inert atmosphere for long-time operation. It should be noted that by making use of the drop-dispensing device, the waste of material required for preparation of the detectors is close to zero. In comparison, by inkjet printing materials are lost in the head space of the print head, and by spin coating or doctor blade casting substrate areas are covered, including the parts which are not used by the detector devices. For each detector demonstrated here, the amount of used material was less than 6 mg/cm<sup>2</sup>, so even for commercially purchased nanocrystals and other inks, the material costs for an infrared detector will be below 20 cents per square centimeter. The low material costs, together with the fast and scalable processing, makes these detectors attractive for large-scale applications, including integration into customized read-out electronics.

## CONCLUSIONS

While PbS-based nanocrystal devices have been discussed in literature for more than a decade, and regular progress is reported with respect to device performances and nanocrystal processing,<sup>41,51–58</sup> here, we have demonstrated two strategies for obtaining all-printed devices with these nanocrystals as photosensitive material. While the first attempt based on all inkjet printing delivered functional devices, the achieved ink properties disable the up-scaling of their production. Thus, a second approach was developed in which the photosensitive layer were deposited in an automatized way by a robotic system, placing the required amount of nanocrystal solution within a single-step deposition. The obtained devices exhibited a high detectivity of  $\sim 10^{12}$  Jones and a cut-off frequency of 3317 Hz. These properties were achieved due the addition of a polymer to the nanocrystal ink, offering coordination groups. The addition of PVP to the ink resulted in an increased colloidal stability of the nanocrystal ink, substantially improving film-forming properties and improving photo-responsivity spectra. At the end, the detectivity of the photoconductors with PVP was clearly improved with respect to those without PVP. These findings might be not only restricted to photoconductors but also are certainly transferable to other device architectures in which film quality is essential, such as thin film transistors or photovoltaic cells (promising results of a first, non-optimized photodiode with the PbS ink as photoactive layer is demonstrated in Figure S15). The automated single-drop deposition of fully active layers is certainly of interest due to economic reasons because it is material- and labor-saving and thus easily scalable to large areas and device quantities, these qualities being another drive toward cost-effective optoelectronics.

## METHODS

**Printing of Ag Electrodes and ZnO Nanocrystal Film.** All devices were fabricated on float glass sheets from Weidner Glas. The substrates were cleaned by rinsing in DI water and sonicating in acetone (technical grade >99%, Chemsolute) and in isopropanol (technical grade >99%, Chemsolute) for 15 min for each step. The printing of the electrodes was performed by a laboratory-scale printer PiXDRO LP50 from Roth and Rau using an industrial print head (Spectra SE 128, 128 nozzles, native resolution of 50 dpi). Interdigitated Ag electrodes were printed using a nanoparticle ink (Sicrys I40TM-106 from PV Nano Cell). After curing in ambient atmosphere, the layers achieved a sheet resistance of less than 1 Ω/□ (thickness of  $\sim 500$  nm). As a protection layer, a ZnO nanoparticle dispersion (N-10 from Nanograde) was modified with 2-propanediol (Sigma-Aldrich) and deposited by inkjet printing to obtain a uniform film with a thickness of  $\sim 20$  nm.

**PbS Ink Preparation.** Oleic acid capped PbS nanocrystals synthesized in an industrial continuous flow reaction were provided by CAN GmbH Hamburg. For ligand exchange, first, inside a glove box, an anhydrous DMF solution of MAI and BiI<sub>3</sub> in a molar ratio of 3:1 was prepared to form iodobismuthate complexes. A total of 24 mL of this mixture containing 6.5 wt % of MAI-BiI<sub>3</sub> reactants was added to 10 mL of 20 mg/mL PbS nanocrystals in hexane. After shaking for 10 s and waiting for phase separation, the nanocrystals were extracted from the hexane phase (upper) into the DMF (lower) solution. The hexane layer was removed using a pipet, and 40 mL of anhydrous hexane was added. After shaking for 15 s again and waiting for phase separation, the hexane was removed. This anhydrous hexane rinsing was performed twice, followed by addition of 32 mL of anhydrous toluene and centrifugation at 6000 rpm for 5 min. The supernatant was discarded, and 8 mL of anhydrous DMF was used to dissolve black solid residue to prepare for the next re-precipitation by adding of 32 mL of anhydrous toluene and centrifugation at 6000 rpm for 5 min. The final solid was dissolved in 5 mL of DMF/NMF/DMSO with a volume ratio of 2:1:1 and filtered through a 0.2 mm Nylon syringe filter. For ink improvement, 5% PVP (Sigma-Aldrich) was added.

**Printing of PbS Nanocrystals.** The PbS inks were printed in a setup including a single MJ-AT printing nozzle (Microfab Technologies) with a 80 μm orifice. For droplet monitoring, stroboscopic illumination by a light-emitting diode was used, synchronized to the pulses applied to the piezoelectric print head. The substrate was moved by a motorized translation stage (Standa, 8MT173) and a step size of 1.25 μm. Stable drop ejection was achieved by proper selection of the electrical drive parameter for the piezo jetting device (applied was a trapezoidal shaped double-pulse with an amplitude of +80 V, a dwell time of 6 μs, and rise and fall times of 4 μs). Pattern formation on the glass substrates was controlled by adjusting the printing frequency at constant stage speed (5 mm/s). The substrate temperature was controlled by a thermoelectric Peltier element. The printed PbS structures were dried for 5 min at 80 °C. The viscosity was measured by rheometer (HAAKE RheoStress 6000, ThermoScientific). The surface tension was measured by the pendant-drop method with a USB DP-M17 9MP digital microscope camera.

**Device Preparation by Droplet Dispensing.** Prior to the droplet dispensing, frames were fabricated from hydrophobic ABS (Renkforce) by using an industrial 3D printer (Ultimaker 2d+). For the deposition of the PbS nanocrystal ink within ABS frames a Freedom Evo 100 (Tecan Group AG, Switzerland), a pipetting robot was used, whereby the system was handled by the software EVOware Standard (version 2.7). Basically, the robot consists of four separately controllable pipetting channels (volume range per channel: 0.1–1000 μL) mounted on a moving arm. For our studies, volumes of 8 and 15 μL were used for the small-area (Figure 5a) and large-area detectors (Figure S10), respectively, with a pipetting speed of 600 μL/s.

**Topographic Characterizations.** A confocal microscope from NanoFocus was used to measure height profiles from printed nanocrystal test devices. The thickness of the printed nanocrystal

lines and ridges were determined by atomic force microscopy conducted in ambient atmosphere with a Veeco Dimension 3100 together with the Veeco NanoScope V controller for high-resolution imaging. The samples were measured in tapping mode with a silicon tip with a nominal tip radius of 7 nm. Furthermore, for simple film thickness measurements, a Tencor profilometer was employed.

**Electro-optical Device Characterization.** Sheet resistance measurements were performed on the silver films with a four-point probe R-Check from EDTM. All of the photoconducting devices were operated at room temperature and under ambient atmosphere. For current–voltage measurements with and without illumination, a Keithley 236 SMU was used. The photocurrent spectra were recorded by making use of a lock-in amplifier from Stanford Research (SR510), with which the noise current was also measured. As an illumination source, we used a tungsten lamp modulated by a mechanical chopper. The light was monochromatized through an Acton SP2150 (Princeton Instruments) combination spectrograph and monochromator.

## ASSOCIATED CONTENT

### Supporting Information

The Supporting Information is available free of charge on the ACS Publications website at DOI: 10.1021/acs.nano.8b09223.

Figures showing ink properties and characteristics of the printed devices (PDF)

Supporting movie showing the printing of a detector array (MP4)

## AUTHOR INFORMATION

### Corresponding Author

\*E-mail: [Wolfgang.Heiss@fau.de](mailto:Wolfgang.Heiss@fau.de).

### ORCID

Marcus Halik: 0000-0001-5976-0862

Wolfgang Heiss: 0000-0003-0430-9550

### Present Address

<sup>V</sup>Zentrum für Angewandte Nanotechnologie CAN, Fraunhofer Institut für Angewandte Polymerforschung IAP, Geiselbergstraße 69, 14476 Potsdam-Golm, Germany

### Author Contributions

The manuscript was written through contributions of all authors. All authors have given approval to the final version of the manuscript.

### Notes

The authors declare no competing financial interest.

## ACKNOWLEDGMENTS

A part of the research was performed at the Energie Campus Nürnberg and supported by funding through the “Aufbruch Bayern” initiative of the state of Bavaria. N.K. acknowledges support by the European Research Council *via* the Marie Skłodowska Curie action Phonsi (grant no. H2020-MSCA-ITN-642656). A.A.J.A. thanks the “Österreichische Forschungsförderungsgesellschaft” FFG for financial support *via* the project Real Nano (project no. 843598). M.S. acknowledges funds from the “Deutsche Forschungsgemeinschaft” (DFG) through the Cluster of Excellence “Engineering of Advanced Materials (EAM)” project EXC315 of the University Erlangen-Nürnberg.

## REFERENCES

(1) Adams, J. J.; Duoss, E. B.; Malkowski, T. F.; Motala, M. J.; Ahn, B. Y.; Nuzzo, R. G.; Bernhard, J. T.; Lewis, J. A. Conformal Printing of

Electrically Small Antennas on Three-Dimensional Surfaces. *Adv. Mater.* **2011**, *23*, 1335–1340.

(2) Liang, J.; Chiau, C. C.; Chen, X.; Parini, C. G. Study of a Printed Circular Disc Monopole Antenna for UWB Systems. *IEEE Trans. Antennas Propag.* **2005**, *53*, 3500–3504.

(3) Vyas, R.; Lakafosis, V.; Lee, H.; Shaker, G.; Yang, L.; Orecchini, G.; Traile, A.; Tentzeris, M. M.; Roselli, L. Inkjet Printed, Self Powered, Wireless Sensors for Environmental, Gas, and Authentication-Based Sensing. *IEEE Sens. J.* **2011**, *11*, 3139–3152.

(4) Khan, S.; Lorenzelli, L.; Dahiya, R. S. Technologies for Printing Sensors and Electronics over Large Flexible Substrates: A Review. *IEEE Sens. J.* **2015**, *15*, 3164–3185.

(5) Sekine, T.; Sugano, R.; Tashiro, T.; Sato, J.; Takeda, Y.; Matsui, H.; Kumaki, D.; Dos Santos, F. D.; Miyabo, A.; Tokito, S. Fully Printed Wearable Vital Sensor for Human Pulse Rate Monitoring Using Ferroelectric Polymer. *Sci. Rep.* **2018**, *8*, 1–10.

(6) Abellán-Llobregat, A.; Jeerapan, I.; Bhandarkar, A.; Vidal, L.; Canals, A.; Wang, J.; Morallón, E. A Stretchable and Screen-Printed Electrochemical Sensor for Glucose Determination in Human Perspiration. *Biosens. Bioelectron.* **2017**, *91*, 885–891.

(7) Trung, T. Q.; Lee, N. E. Flexible and Stretchable Physical Sensor Integrated Platforms for Wearable Human-Activity Monitoring and Personal Healthcare. *Adv. Mater.* **2016**, *28*, 4338–4372.

(8) Park, J. S.; Kim, T. W.; Stryakhilev, D.; Lee, J. S.; An, S. G.; Pyo, Y. S.; Lee, D. B.; Mo, Y. G.; Jin, D. U.; Chung, H. K. Flexible Full Color Organic Light-Emitting Diode Display on Polyimide Plastic Substrate Driven by Amorphous Indium Gallium Zinc Oxide Thin-Film Transistors. *Appl. Phys. Lett.* **2009**, *95*, 2007–2010.

(9) Sekitani, T.; Nakajima, H.; Maeda, H.; Fukushima, T.; Aida, T.; Hata, K.; Someya, T. Stretchable Active-Matrix Organic Light-Emitting Diode Display Using Printable Elastic Conductors. *Nat. Mater.* **2009**, *8*, 494–499.

(10) Berggren, M.; Nilsson, D.; Robinson, N. D. Organic Materials for Printed Electronics. *Nat. Mater.* **2007**, *6*, 3.

(11) Teichler, A.; Perelaer, J.; Schubert, U. S. Inkjet Printing of Organic Electronics-Comparison of Deposition Techniques and State-of-the-Art Developments. *J. Mater. Chem. C* **2013**, *1*, 1910–1925.

(12) Kamysnyh, A.; Magdassi, S. Conductive Nanomaterials for Printed Electronics. *Small* **2014**, *10*, 3515–3535.

(13) Lee, K. J.; Jun, B. H.; Kim, T. H.; Joung, J. Direct Synthesis and Inkjetting of Silver Nanocrystals toward Printed Electronics. *Nanotechnology* **2006**, *17*, 2424–2428.

(14) Kamysnyh, A. Metal-Based Inkjet Inks for Printed Electronics. *Open Appl. Phys. J.* **2011**, *4*, 19–36.

(15) Ridley, B. A.; Nivi, B.; Jacobson, J. M. All-Inorganic Field Effect Transistors Fabricated by Printing. *Science* **1999**, *286*, 746–750.

(16) Panthani, M. G.; Akhavan, V.; Goodfellow, B. W.; Schmidtke, J. P.; Dunn, L.; Dodabalapur, A.; Barbara, P. F.; Korgel, B. a. Nanocrystal “Inks” for Printable Photovoltaics. *J. Am. Chem. Soc.* **2008**, *130*, 16770–16777.

(17) Böberl, M.; Kovalenko, M. V.; Gamerith, S.; List, E. J. W.; Heiss, W. Inkjet-Printed Nanocrystal Photodetectors Operating up to 3 Mm Wavelengths. *Adv. Mater.* **2007**, *19*, 3574–3578.

(18) Dirin, D. N.; Dreyfuss, S.; Bodnarchuk, M. I.; Nedelcu, G.; Papagiorgis, P.; Itskos, G.; Kovalenko, M. V. Lead Halide Perovskites and Other Metal Halide Complexes as Inorganic Capping Ligands for Colloidal Nanocrystals. *J. Am. Chem. Soc.* **2014**, *136*, 6550–6553.

(19) Zhang, H.; Jang, J.; Liu, W.; Talpin, D. V. Colloidal Nanocrystals with Inorganic Halide, Pseudohalide, and Halometallate Ligands. *ACS Nano* **2014**, *8*, 7359–7369.

(20) Aqoma, H.; Al Mubarak, M.; Hadmojo, W. T.; Lee, E. H.; Kim, T. W.; Ahn, T. K.; Oh, S. H.; Jang, S. Y. High-Efficiency Photovoltaic Devices Using Trap-Controlled Quantum-Dot Ink Prepared *via* Phase-Transfer Exchange. *Adv. Mater.* **2017**, *29*, 1605756.

(21) Fan, J. Z.; Liu, M.; Voznyy, O.; Sun, B.; Levina, L.; Quintero-Bermudez, R.; Liu, M.; Ouellette, O.; García De Arquer, F. P.; Hoogland, S.; Sargent, E. H. Halide Re-Shelled Quantum Dot Inks for

Infrared Photovoltaics. *ACS Appl. Mater. Interfaces* **2017**, *9*, 37536–37541.

(22) Yang, Z.; Fan, J. Z.; Proppe, A. H.; De Arquer, F. P. G.; Rossouw, D.; Voznyy, O.; Lan, X.; Liu, M.; Walters, G.; Quintero-Bermudez, R.; Sun, B.; Hoogland, S.; Botton, G. A.; Kelley, S. O.; Sargent, E. H. Mixed-Quantum-Dot Solar Cells. *Nat. Commun.* **2017**, *8*, 1–8.

(23) Balazs, D. M.; Rizkia, N.; Fang, H. H.; Dirin, D. N.; Momand, J.; Kooi, B. J.; Kovalenko, M. V.; Loi, M. A. Colloidal Quantum Dot Inks for Single-Step-Fabricated Field-Effect Transistors: The Importance of Postdeposition Ligand Removal. *ACS Appl. Mater. Interfaces* **2018**, *10*, 5626–5632.

(24) Sytnyk, M.; Yakunin, S.; Schöfberger, W.; Lechner, R. T.; Burian, M.; Ludescher, L.; Killilea, N. A.; Yousefiamin, A.; Kriegner, D.; Stangl, J.; Groiss, H.; Heiss, W. Quasi-Epitaxial Metal-Halide Perovskite Ligand Shells on PbS Nanocrystals. *ACS Nano* **2017**, *11*, 1246–1256.

(25) Downs, C.; Vandervelde, T. E. *Progress in Infrared Photo-detectors Since 2000* **2013**, *13* (4), 5054.

(26) Maisch, P.; Tam, K. C.; Lucera, L.; Egelhaaf, H. J.; Scheiber, H.; Maier, E.; Brabec, C. J. Inkjet Printed Silver Nanowire Percolation Networks as Electrodes for Highly Efficient Semitransparent Organic Solar Cells. *Org. Electron.* **2016**, *38*, 139–143.

(27) Lenz, T.; Richter, M.; Matt, G. J.; Luechinger, N. A.; Halim, S. C.; Heiss, W.; Brabec, C. J. Charge Transport in Nanoparticle Thin Films of Zinc Oxide and Aluminum-Doped Zinc Oxide. *J. Mater. Chem. C* **2015**, *3*, 1468–1472.

(28) Manor, A.; Katz, E. A.; Tromholt, T.; Krebs, F. C. Enhancing Functionality of ZnO Hole Blocking Layer in Organic Photovoltaics. *Sol. Energy Mater. Sol. Cells* **2012**, *98*, 491–493.

(29) Hadouchi, W.; Rousset, J.; Tondelier, D.; Geffroy, B.; Bonnassieux, Y. Zinc Oxide as a Hole Blocking Layer for Perovskite Solar Cells Deposited in Atmospheric Conditions. *RSC Adv.* **2016**, *6*, 67715–67723.

(30) Weidman, M. C.; Yager, K. G.; Tisdale, W. A. Interparticle Spacing and Structural Ordering in Superlattice PbS Nanocrystal Solids Undergoing Ligand Exchange. *Chem. Mater.* **2015**, *27*, 474–482.

(31) Balazs, D. M.; Dirin, D. N.; Fang, H. H.; Protesescu, L.; Ten Brink, G. H.; Kooi, B. J.; Kovalenko, M. V.; Loi, M. A. Counterion-Mediated Ligand Exchange for PbS Colloidal Quantum Dot Superlattices. *ACS Nano* **2015**, *9*, 11951–11959.

(32) Brown, P. R.; Kim, D.; Lunt, R. R.; Zhao, N.; Bawendi, M. G.; Grossman, J. C.; Bulović, V. Energy Level Modification in Lead Sulfide Quantum Dot Thin Films through Ligand Exchange. *ACS Nano* **2014**, *8*, 5863–5872.

(33) Chuang, C.-H. M.; Brown, P. R.; Bulović, V.; Bawendi, M. G. Improved Performance and Stability in Quantum Dot Solar Cells through Band Alignment Engineering. *Nat. Mater.* **2014**, *13*, 796–801.

(34) Crisp, R. W.; Kroupa, D. M.; Marshall, A. R.; Miller, E. M.; Zhang, J.; Beard, M. C.; Luther, J. M. Metal Halide Solid-State Surface Treatment for High Efficiency PbS and PbSe QD Solar Cells. *Sci. Rep.* **2015**, *5*, 1–6.

(35) Bernal-García, J. M.; Guzmán-López, A.; Cabrales-Torres, A.; Estrada-Baltazar, A.; Iglesias-Silva, G. A. Densities and Viscosities of (N, N -Dimethylformamide + Water) at Atmospheric Pressure from (283.15 to 353.15) K. *J. Chem. Eng. Data* **2008**, *53*, 1024–1027.

(36) Ciocirlan, O.; Iulian, O. Density, Viscosity and Refractive Index of the Dimethyl Sulfoxide + o-Xylene System. *J. Serb. Chem. Soc.* **2009**, *74*, 317–329.

(37) Toda, K.; Furuse, H. Extension of Einstein's Viscosity Equation to That for Concentrated Dispersions of Solutes and Particles. *J. Biosci. Bioeng.* **2006**, *102*, 524–528.

(38) McKinley, G. H.; Renardy, M. Wolfgang von Ohnesorge. *Phys. Fluids* **2011**, *23*, 127101.

(39) Soltman, D.; Subramanian, V. Inkjet-Printed Line Morphologies and Temperature Control of the Coffee Ring Effect. *Langmuir* **2008**, *24*, 2224–2231.

(40) Karapetsas, G.; Matar, O. K.; Valluri, P.; Sefiane, K. Convective Rolls and Hydrothermal Waves in Evaporating Sessile Drops. *Langmuir* **2012**, *28*, 11433–11439.

(41) Konstantatos, G.; Howard, I.; Fischer, A.; Hoogland, S.; Clifford, J.; Klem, E.; Levina, L.; Sargent, E. H. Ultrasensitive Solution-Cast Quantum Dot Photodetectors. *Nature* **2006**, *442*, 180–183.

(42) Guo, Y.; Shoyama, K.; Sato, W.; Nakamura, E. Polymer Stabilization of Lead(II) Perovskite Cubic Nanocrystals for Semi-transparent Solar Cells. *Adv. Energy Mater.* **2016**, *6*, 1–9.

(43) Li, B.; Zhang, Y.; Fu, L.; Yu, T.; Zhou, S.; Zhang, L.; Yin, L. Surface Passivation Engineering Strategy to Fully-Inorganic Cubic CsPbI<sub>3</sub>perovskites for High-Performance Solar Cells. *Nat. Commun.* **2018**, *9*, 1–8.

(44) Szendrei, K.; Gomulya, W.; Yarema, M.; Heiss, W.; Loi, M. A. PbS Nanocrystal Solar Cells with High Efficiency and Fill Factor. *Appl. Phys. Lett.* **2010**, *97*, 2–5.

(45) Stadler, P.; Mohamed, S. a.; Gasiorowski, J.; Sytnyk, M.; Yakunin, S.; Scharber, M. C.; Enengl, C.; Enengl, S.; Egbe, D. a M.; El-Mansy, M. K.; Obayya, S. S. A.; Sariciftci, N. S.; Hingerl, K.; Heiss, W. Iodide-Capped PbS Quantum Dots : Full Optical Characterization of a Versatile Absorber. *Adv. Mater.* **2015**, *27*, 1533–1539.

(46) Brown, P. R.; Lunt, R. R.; Zhao, N.; Osedach, T. P.; Wanger, D. D.; Chang, L.; Bawendi, M. G.; Bulović, V. Improved Current Extraction from ZnO/PbS Quantum Dot Heterojunction Photovoltaics Using a MoO<sub>3</sub> Interfacial Layer. *Nano Lett.* **2011**, *11*, 2955–2961.

(47) Hu, C.; Gassenq, A.; Justo, Y.; Devloo-Casier, K.; Chen, H.; Detavernier, C.; Hens, Z.; Roelkens, G. Air-Stable Short-Wave Infrared PbS Colloidal Quantum Dot Photoconductors Passivated with Al<sub>2</sub>O<sub>3</sub> Atomic Layer Deposition. *Appl. Phys. Lett.* **2014**, *105*, 171110.

(48) Yakunin, S.; Dirin, D. N.; Protesescu, L.; Sytnyk, M.; Tollabimazraehno, S.; Humer, M.; Hackl, F.; Fromherz, T.; Bodnarchuk, M. I.; Kovalenko, M. V.; Heiss, W. High Infrared Photoconductivity in Films of Arsenic-Sulfide-Encapsulated Lead-Sulfide Nanocrystals. *ACS Nano* **2014**, *8*, 12883–12894.

(49) Szendrei, K.; Cordella, F.; Kovalenko, M. V.; Böberl, M.; Hesser, G.; Yarema, M.; Jarzab, D.; Mikhnenko, O. V.; Gocalinska, A.; Saba, M.; Quochi, F.; Mura, A.; Bongiovanni, G.; Blom, P.; Heiss, W.; Loi, M. A. Solution-Processable near-IR Photodetectors Based on Electron Transfer from PbS Nanocrystals to Fullerene Derivatives. *Adv. Mater.* **2009**, *21*, 683–687.

(50) De Iacovo, A.; Venettacci, C.; Colace, L.; Scopa, L.; Foglia, S. PbS Colloidal Quantum Dot Photodetectors Operating in the near Infrared. *Sci. Rep.* **2016**, *6*, 1–9.

(51) Tang, J.; Sargent, E. H. Infrared Colloidal Quantum Dots for Photovoltaics: Fundamentals and Recent Progress. *Adv. Mater.* **2011**, *23*, 12–29.

(52) McDonald, S. A.; Konstantatos, G.; Zhang, S.; Cyr, P. W.; Klem, E. J. D.; Levina, L.; Sargent, E. H. Solution-Processed PbS Quantum Dot Infrared Photodetectors and Photovoltaics. *Nat. Mater.* **2005**, *4*, 138–142.

(53) Bakueva, L.; Musikhin, S.; Hines, M. A.; Chang, T. W. F.; Tzolov, M.; Scholes, G. D.; Sargent, E. H. Size-Tunable Infrared (1000–1600 Nm) Electroluminescence from PbS Quantum-Dot Nanocrystals in a Semiconducting Polymer. *Appl. Phys. Lett.* **2003**, *82*, 2895–2897.

(54) Saran, R.; Curry, R. J. Lead Sulphide Nanocrystal Photodetector Technologies. *Nat. Photonics* **2016**, *10*, 81–92.

(55) Kovalenko, M. V.; Manna, L.; Cabot, A.; Hens, Z.; Talapin, D. V.; Kagan, C. R.; Klimov, V. I.; Rogach, A. L.; Reiss, P.; Milliron, D. J.; Guyot-Sionnest, P.; Konstantatos, G.; Parak, W. J.; Hyeon, T.; Korgel, B. A.; Murray, C. B.; Heiss, W. Prospects of Nanoscience with Nanocrystals. *ACS Nano* **2015**, *9*, 1012–1057.

(56) Hendricks, M. P.; Campos, M. P.; Cleveland, G. T.; Jen-La Plante, I.; Owen, J. S. A Tunable Library of Substituted Thiourea Precursors to Metal Sulfide Nanocrystals. *Science* **2015**, *348*, 1226–1230.

(57) Bozyigit, D.; Lin, W. M. M.; Yazdani, N.; Yarema, O.; Wood, V. A Quantitative Model for Charge Carrier Transport, Trapping and Recombination in Nanocrystal-Based Solar Cells. *Nat. Commun.* **2015**, *6*, 1–10.

(58) Zherebetsky, D.; Scheele, M.; Zhang, Y.; Bronstein, N.; Thompson, C.; Britt, D.; Salmeron, M.; Alivisatos, P.; Wang, L. W. Hydroxylation of the surface of PbS nanocrystals passivated with oleic acid. *Science* **2014**, *344*, 1380–1384.